



HAL
open science

Full-silica metamaterial wave plate for high-intensity UV lasers

Nicolas Bonod, Pierre Brianceau, Jérôme Neauport

► **To cite this version:**

Nicolas Bonod, Pierre Brianceau, Jérôme Neauport. Full-silica metamaterial wave plate for high-intensity UV lasers. *Optica*, 2021, 8 (11), pp.1372. 10.1364/OPTICA.434662 . hal-03410617

HAL Id: hal-03410617

<https://hal.science/hal-03410617>

Submitted on 1 Nov 2021

HAL is a multi-disciplinary open access archive for the deposit and dissemination of scientific research documents, whether they are published or not. The documents may come from teaching and research institutions in France or abroad, or from public or private research centers.

L'archive ouverte pluridisciplinaire **HAL**, est destinée au dépôt et à la diffusion de documents scientifiques de niveau recherche, publiés ou non, émanant des établissements d'enseignement et de recherche français ou étrangers, des laboratoires publics ou privés.



Distributed under a Creative Commons Attribution 4.0 International License



Full-silica metamaterial wave plate for high-intensity UV lasers

NICOLAS BONOD,¹ PIERRE BRIANCEAU,² AND JÉRÔME NEAUPORT^{3,*} 

¹Aix-Marseille University, CNRS, Centrale Marseille, Institut Fresnel, 13013 Marseille, France

²CEA-GRENOBLE, F-38054, Grenoble Cedex, France

³CEA-CESTA, 15 Avenue des Sablières, CS 60001, F-33116, Le Barp Cedex, France

*Corresponding author: jerome.neauport@cea.fr

Received 21 June 2021; revised 2 September 2021; accepted 7 September 2021 (Doc. ID 434662); published 26 October 2021

Bringing light–matter interactions into novel standards of high-energy physics is a major scientific challenge that motivated the funding of ambitious international programs to build high-power laser facilities. The major issue to overcome is to avoid laser intensity heterogeneities over the target that weaken the light–matter interaction strength. Laser beam smoothing aims at homogenizing laser intensities by superimposing on the target laser speckle intensities produced by orthogonal left and right circularly polarized beams. Conventional wave plates based on anisotropic crystals cannot support the laser fluences of such lasers, and the challenge is now to design wave plates exhibiting a high laser induced damage threshold (LIDT). Fused silica exhibits high LIDT, but its isotropic dielectric permittivity prevents effects on polarization retardance. Metamaterials have been widely investigated to tailor the phase and polarization of light but with plasmonic or high-refractive-index materials, and applying this approach with silica is highly challenging due to the weak optical contrast between silica and air or vacuum. Here we design and fabricate a silica-based metasurface acting almost like a quarter-wave plate in the UV spectral range, fulfilling the numerous constraints inherent to high-power laser beamlines, in particular, high LIDT and large sizes. We numerically and experimentally demonstrate that fused silica etched by deep grooves with a period shorter than the wavelength at 351 nm operates the linear-to-quasi circular polarization conversion together with a high transmission efficiency and a high LIDT. The high aspect ratio of the grooves due to the short period imposed by the short wavelength and the deepness of the grooves required to overcome the weak optical contrast between silica and air is experimentally obtained through a CMOS compatible process. © 2021 Optical Society of America under the terms of the [OSA Open Access Publishing Agreement](https://doi.org/10.1364/OPTICA.434662)

<https://doi.org/10.1364/OPTICA.434662>

1. INTRODUCTION

Large power laser facilities such as NIF [1], LMJ [2], OMEGA [3,4] or SG-III laser [5] have been developed to bring matter to extreme conditions of pressure and temperature by the interaction of multiple ultraviolet (UV) nanosecond laser beams on a small target composed of a centimeter gold capsule. The major challenge for bringing the light–matter interaction to extreme levels is to yield homogeneous laser focused beams around the capsule. The laser coherence yields speckle grains in the focused beam that modulate laser intensity and bring heterogeneities of laser intensity around the target. During the light–matter interaction, laser intensity heterogeneity can lead to the formation of laser-plasma instabilities such as stimulated Raman and Brillouin scattering, self-focusing, and filamentation that further affect the quality of the laser beam by inducing an additional heterogeneity in intensity. To solve this major issue, various laser beam smoothing techniques have therefore been developed in both time and spatial domains such as smoothing by spectral dispersion (SSD) [6,7], phase plates [8–10], or polarization smoothing (PS) [11–13].

High-power laser facilities usually combine both time and spatial domain techniques. SSD, in its different forms, is performed by using a phase modulator to broaden the spectrum of the laser. The frequencies are then dispersed by a diffraction grating producing speckles spatially shifted after focusing. The result is a reduction in contrast of the focal spot intensity pattern over time. The envelope of the focal spot is finally determined by a phase plate placed either before or after focusing. Additional contrast reduction can be obtained with PS, which aims at smoothing laser intensity in the spatial domain. This technique is based on the use of a birefringent optical component that creates two orthogonal states of polarization. The orthogonality of the two beams avoids interference effects of the two coherent beams. The laser intensity patterns are therefore added around the target, which reduces the contrast by an amount of $\sqrt{2}$. A better balance of polarizations, needed in the context of direct drive, can also be obtained with the use of random continuous polarization plates [14]. While the SSD approach is time dependent, i.e., smooths intensity patterns in the time domain, PS is instantaneous and smooths intensity patterns in the spatial domain. This latter approach turns out to be highly suitable for high-power laser pulses since it is instantaneous and

therefore reduces instabilities, whatever the time-dependent beam smoothing strategy retained.

Birefringent crystals are usually used to create two orthogonal linear polarizations. When a large-sized optical component is needed, as is the case for the aforementioned laser facilities, potassium dihydrogen phosphate (KDP) is preferred since it is the only crystal available in large volumes. Different configurations are used such as wedge KDP in collimated beams [11,12,15], half-wave KDP plates in collimated beams [16], or KDP scrambler in convergent beams [17,18]. When KDP crystals are positioned after the frequency conversion stage, i.e., at the wavelength of 351 nm, they face two main limitations: transverse stimulated Raman scattering (TSRS) and laser damage resistance. KDP exhibits a relatively high Raman gain at 351 nm [19], which can trigger Raman scattering, this Raman signal being further amplified along the crystalline optic transverse direction when a large KDP crystal is exposed to high intensities in the UV. This effect can be reduced by adding deuterium, thus replacing KDP by DKDP, but it is still deleterious in some specific configurations resulting in losses of the main beam energy and even damage of KDP/DKDP optics [20]. Important developments are still carried out to overcome this TSRS limitation [21,22]. However, the laser damage resistance of KDP/DKDP at the wavelength of 351 nm, even when enhanced by laser conditioning [20], remains significantly smaller than that of fused silica. Alternative materials are being developed such as liquid crystals [23] or glancing angle deposition coatings [24], but none of them has actually come to a sufficient level of maturity to be used in a fusion class laser facility.

Here we propose and investigate a novel approach of beam smoothing based on the use of silica-based metasurfaces acting almost like a quarter-wave plate for converting in the UV spectral range a linear polarization into a quasi-circular polarization. The orientation of the fast axis of the metasurfaces compared with the linear polarization of the incident beam will determine the left or right orientation of circular polarization. Metasurfaces will be placed at the final stage of the laser chain, i.e., after the amplification stage and nonlinear conversion of the frequency, which means that they will tailor laser beams at 3ω for which $\lambda = 351$ nm. This objective requires the design and fabrication of a metasurface in fused silica with nanostructures scaling with the short wavelength $\lambda = 351$ nm.

The design and fabrication of large scale metasurfaces operating at the final stage of high-power laser chains raise several specific challenges that need to be addressed. (i) The optical metasurfaces being implemented where the laser beams have gained their maximal power need to exhibit high laser induced damage thresholds (LIDTs). That is the reason why we consider fused silica as the unique optical material to design such optical wave plates. (ii) While most optical metasurfaces are composed of optical materials that yield high optical contrasts, e.g., plasmonics or high-refractive-index dielectric materials [25–33], here we have to design wave plates with fused silica whose small refractive index n , $n \approx 1.47$, yields a weak optical contrast with air. (iii) The surface of the optical metasurfaces has to match the large area of the laser beams. In the case of the LMJ project, the laser beams feature a 40×40 cm² area. The fabrication technique selected for etching silica-based metasurfaces has to be compatible with large scale processes. (iv) The metasurface operates in the UV spectral range at $\lambda = 351$ nm. This short wavelength brings additional challenges since the scale of the nanostructuring has to be adapted to this short

wavelength, which further increases the mismatch between the scale of fused silica structuring and the scale of the large optics. (v) Laser beam smoothing aims at improving light–matter interactions, and the linear-to-circular polarization conversion has to be associated with a high transmission efficiency.

2. DESIGN

The wave plate metamaterial is composed of fused silica periodically etched with linear grooves. It is modeled with a differential method that is particularly well suited to model periodic optical components [34]. Substrate and pillars are made of fused silica, the superstrate and grooves being filled with air or vacuum, both associated with a refractive index of one. The wave plate operates in transmission and in normal incidence at $\lambda = 351$ nm. The challenge is to associate a polarization conversion corresponding to a retardance greater than $\lambda/5$, ideally $\lambda/4$, with a high transmission of the laser beam through the optical metasurface. We consider linear grooves in fused silica. The groove direction defines the orientation of the fast axis of the wave plate. The groove profile is modeled by a trapezoidal shape, and the angle of inclination of the grooves is taken equal to $\alpha = 87.5^\circ$, in agreement with the images of the samples obtained by electronic microscopy (see Section 4.A). The incident beam is linearly polarized and illuminates the component at normal incidence with the electric field oriented at 45° from the fast axis [see Fig. 1(a)]. The wave plate requires a difference of phase of the electric field components along the fast and low axes transmitted in the zeroth order larger than $\lambda/5$. This property on linear retardance must be associated with an equal and high transmittance of these two components, close to one, to bring almost all the incident energy transmitted through the wave plate to the target.

In the following, we consider transmission efficiencies averaged over the fast and low axes, $T^0 = \frac{1}{2}[T_{\text{fast}}^0 + T_{\text{slow}}^0]$, to calculate the electric field components parallel or normal to the fast axis. The groove width at mid-height is denoted c , and the duty cycle (DC) $DC = 1 - \frac{c}{d}$. The index of refraction of fused silica is set to 1.47605 at the wavelength of 351 nm. We set the period at $d = 260$ nm for minimizing the propagation of energy in the non-specular $\pm 1^{\text{st}}$ orders. DCs are set close to $DC = 0.4$ to be in agreement with the technological fabrication constraints. We perform numerical simulations to calculate the transmission efficiency in the zeroth order and the difference of phase $\Delta\phi$ between the electric fields transmitted through the zeroth order for an electric field parallel or normal to the fast axis.

We represent in Figs. 1(b) and 1(c) the averaged transmission efficiencies T^0 and the fraction of the wavelength corresponding to the difference of phase $\frac{2\pi}{\Delta\phi}$ with respect to the period d and the groove depth h . It can be clearly observed that short periods are required to prevent energy to propagate through non-specular orders and to maximize transmittance in the specular order. A period of 260 nm allows for getting transmission efficiencies T^0 larger than 93%. This is the period that will be chosen for fabrication of the samples. If T^0 has strong sensitivity on the period and weak sensitivity on the groove depth, the difference of phase induced by the metamaterial wave plate $\Delta\phi$ features an opposite trend with weak sensitivity on the period and strong sensitivity on the groove depth. Significant phase retardances induced by the wave plate, typically larger than $\lambda/5$, require groove depths larger than 750 nm, preferentially larger than 800 nm and ideally

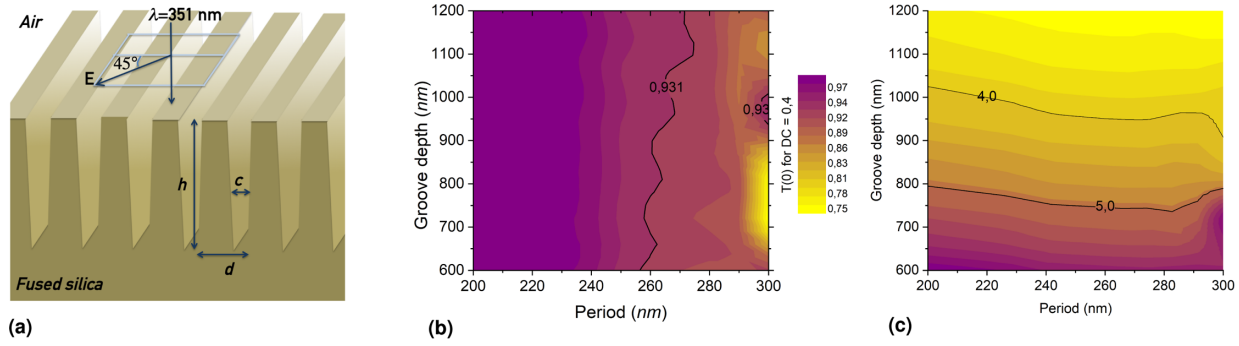


Fig. 1. Numerical design of a silica-based UV quarter-wave plate. (a) Schematic representation of the periodically nanostructured glass with groove depth h and groove width at mid-height c . The substrate is made of glass with an index of refraction of 1.47605, and the superstrate is made of air. The incoming beam has a normal incidence, and a linear polarization with an electric field oriented at 45° from the orientation of the grooves. Wavelength is $\lambda = 351$ nm. (b) Transmission efficiency T^0 in the zeroth order averaged over both polarizations $T^0 = \frac{1}{2}[T_{TE}^0 + T_{TM}^0]$ with respect to the period d and the groove depth for a duty cycle $DC = 0.4$; high transmission, larger than 93%, is obtained for periods smaller than 260 nm. (c) Difference of phase $\Delta\phi$ induced by the metamaterial wave plate expressed in terms of λ/x , by plotting $x = 2\pi/\Delta\phi$ with respect to the period d and duty cycle DC for a period of 260 nm. $\Delta\phi$ is obtained by calculating the difference of phase between the transmitted electric field in the zeroth order parallel (TE) or perpendicular (TM) to the fast axis (parallel to the grooves). Significant beam smoothing requires at least a $\lambda/5$ and ideally a $\lambda/4$ metamaterial wave plate; this area of interest is delimited in the figure.

centered around 1000 nm. To catch intuitively the effect of this deeply etched silica material on the phase of light, one calculates the dielectric permittivities of the effective homogeneous uniaxial layer. The extraordinary axis is along the direction of modulation, while the ordinary axes are along the depth of the silica and groove lines. As one does not consider any resonant light scattering to develop this wave plate metasurface, we propose to consider the simple Maxwell-Garnett model, which provides the effective dielectric permittivities $\bar{\epsilon}_o$ and $\bar{\epsilon}_e$ along the ordinary and extraordinary axes by calculating, respectively, the arithmetic and mean values of the dielectric permittivities of silica ϵ_{SiO_2} and air ϵ_{air} [35,36]:

$$\frac{1}{\bar{\epsilon}_e} = \frac{1}{d} \left(\frac{d-c}{\epsilon_{\text{SiO}_2}} + \frac{c}{\epsilon_{\text{air}}} \right), \quad (1)$$

$$\bar{\epsilon}_o = \frac{1}{d} \left((d-c)\epsilon_{\text{SiO}_2} + c\epsilon_{\text{air}} \right). \quad (2)$$

The phase retardance $\overline{\Delta\phi}$ induced by the uniaxial layer of thickness h is obtained through the expression $\Delta\phi = \frac{2\pi h}{\lambda} (\sqrt{\bar{\epsilon}_e} - \sqrt{\bar{\epsilon}_o})$. This allows us to calculate and plot $\overline{\Delta\phi}$ in functions of the groove depth h and DC (see Fig. 2). The phase retardance induced by the uniaxial homogeneous layer features the same trends as that yielded by the metasurface. The optimal thickness for getting a quarter-wave plate is around 1000 nm.

The important result brought by this numerical study is that nanostructured fused silica can simultaneously achieve high transmittance $T^0 > 93\%$ and phase retardance $\Delta\phi \approx \pi/2.5$. The main difficulty to achieve simultaneously these two objectives is that the large groove depth (> 650 nm) is associated with a short period (< 260 nm). This result means that the weak optical contrast between silica and air for tailoring polarization properties of laser beams must be compensated for by a large amplitude of the air/silica modulation obtained with deep grooves. The anti-reflective properties of the wave plate require limiting the spreading of light energy through multiple propagative diffraction orders, which explains why the ratio λ/d has to be ≈ 1.47 . To take into account technological constraints, we select for the fabrication of the samples a period $d = 260$ nm and a groove depth $h = 830$ nm

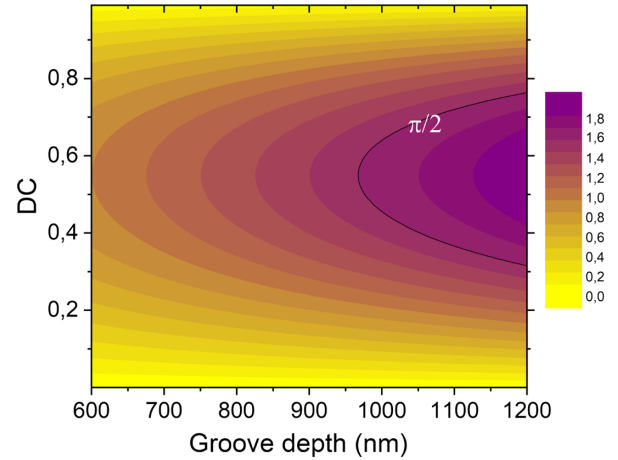


Fig. 2. Phase retardance induced by a uniaxial homogeneous layer as functions of DC and groove depth of the equivalent metasurface.

(with $DC = 0.4$). This set of parameters is expected to yield a transmittance of 93% in the T^0 order and a difference of phase ranging between $\Delta\phi \approx \pi/5$ and $\Delta\phi \approx \pi/4$. The remaining energy is transmitted into the $\pm 1^{\text{st}}$ orders.

3. NANOFABRICATION

Large sub-meter scale gratings used in high-power laser facilities are generally manufactured using either a full-size or sub-aperture holographic recording of a photo-resist layer, a chemical development, followed by an ion etching process [37]. This process flow has turned out to be effective to manufacture moderate quantities of large-sized gratings, but it has also experienced some limitations. In particular, holographic recording induces millimeter to sub-millimeter scale errors that alter the wavefront quality and can impact laser beam propagation [37,38]. The combination of this holographic recording technique and ion etching process can induce localized defects and contamination along the grating lines that can reduce the laser damage resistance of the grating [39–41]. For these reasons, we investigate here the fabrication of

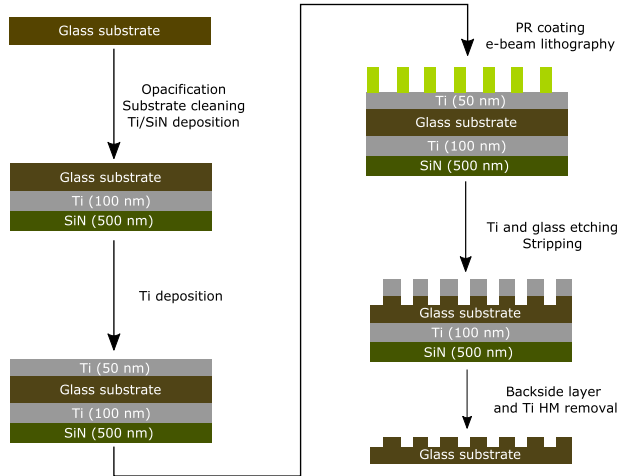


Fig. 3. Metamaterial wave plate process flow. The first step consists of opacifying the back side of the substrate due to the deposition of Ti and SiN layers. A Ti layer is then deposited on the front side. A photo-resistive layer is coated on this latter layer and written by electron beam lithography. A two-step etching process is then used to obtain the final nanostructure.

the metamaterial wave plate using a 200 mm CMOS-compatible fabrication process devoted initially to silicon technologies. Such a process has proven its high accuracy and repeatability in micro-electronics. Figure 3 shows the entire process flow to manufacture the metamaterial wave plates.

Fused silica glass wafers (AQ from AGC Japan) are used as substrates. They have a diameter of $\phi = 200$ mm and thickness of 0.725 mm. We should stress that this wafer thickness is not sufficient to mitigate gravity sag of large-sized laser components. It was selected due to its compatibility with the manufacturing process and because we aim at demonstrating the interest of silica-based metasurfaces for high-power lasers. Substrates are polished and exhibit a surface roughness of less than 2 nm root mean square (RMS) for spatial periods smaller than 1 mm. The metasurface is patterned over a clear aperture of 5×5 cm² centered on the substrate.

A key prerequisite is to make fused silica glass wafers compatible with micro-electronic equipment. Fused silica wafers are transparent in the visible and non-conductive in contrast to silicon wafers. An opacification step is therefore realized to detect wafers with the different equipment sensors (notch aligner, process chamber input and output sensors, etc.) and to allow the de-chucking with the electrostatic chuck. This opacification applied on the back side of the wafers is achieved due to the deposition of two layers, a Ti layer to make wafers opaque and underneath a SiN nitride layer to enable the de-chucking of the wafers (see Fig. 3). After this first opacification step, a Ti layer is deposited on the front glass side. This Ti layer is therefore coated by the photo-resist layer. The patterning of the photo-resist layer is then performed with electron-beam lithography (Variable Shaped Beam SB3054 Model from Vistec). The conductive Ti layer on the front side of the wafer evacuates electrons from the surface of the wafer. This layer has been intentionally increased from 10 nm to 50 nm to act as an additional hard mask to the 360 nm thick photo-resist (NEB22) during the etching of fused silica. This additional hard mask lessens the sidewall roughness and improves the control of the groove width and profile. Scanning electron microscopy (SEM) measurements of the exposed wafer at a dose of $32 \mu\text{C}/\text{cm}^2$ were performed on 25

areas uniformly distributed over the 5×5 cm² grating surface to qualify the uniformity. A linewidth (width of silica pillars on top) of 105.26 nm with an error of 3.97 nm (3σ) is obtained.

The Ti hard mask is then etched in an inductively coupled plasma (ICP) process chamber (AMAT DPSII) due to a two-step recipe. The first step is based on the use of BCl_3 to etch the thin TiO_2 oxidized layer at the surface of the Ti and the second one, based on Cl_2/HBr , to etch the Ti with a selectivity to SiO_2 and photo-resist of about three. Fused silica is then etched in a capacitively coupled plasma (CCP) process chamber (TEL DRM). The plasma recipe is based on $\text{C}_4\text{F}_8/\text{O}_2/\text{CO}/\text{Ar}$ with a selectivity of ~ 5 to the photo-resist and of ~ 8 to Ti. Considering the photo-resist line dimensions, the non-negligible faceting of the resist decreases the selectivity calculated from full-sheet wafers. The use of an additional Ti hard mask reduces the sidewall roughness and helps keep the critical dimensions. Also, an additional *in situ* post-etching treatment (PET) based on O_2/N_2 is performed after fluorocarbon plasma etching to suppress the hard-mask defect formation as the presence of water soluble amines could possibly trigger the formation of TiN surface defects when wafers are exposed to atmosphere. Then, a conventional ashing is performed at 250°C based on O_2/N_2 gas to remove the remaining photo-resist. Afterwards, the opacification layers are removed due to a SF_6/O_2 plasma performed in a manually operated process chamber (CCP NEXUS330). The fused silica wafers are then loaded upside-down on a hollow Si bulk wafer except at the edge to not damage the patterned front side. Finally, a standard cleaning 1 (SC1) process is performed in a wet bench to remove the Ti hard mask on the front side and Ti residues on the back side at the same time.

4. CHARACTERIZATION AND RESULTS

A. Scanning Electron Microscopy

We characterized the morphology of the etched fused silica by SEM (i) to assess the agreement between the structures modeled within the numerical simulations and the trapezoidal profile of the etched grooves, and (ii) to measure the critical dimensions of the nanostructures, lines, and widths, which will be implemented in the numerical code to compare the theoretical optical performances with experimental results. Figure 4 shows SEM cross sections of fused silica nanostructures. We observe the high quality of the groove profile in terms of shape and sharpness of the profile. The profile of the lines features a trapezoidal shape, with a large height compared with a short basis. Importantly, the period and the profile of the nanostructures are constant and homogeneous over 5×5 cm².

Analysis of the SEM images reveals that the depth of the etched grooves ranges between 820 nm and 840 nm. Line and space widths ($d - c$ and c , respectively) differ on the top and bottom of the profile due to a sidewall angle estimated at 87.5° . This angle was taken into account in the numerical simulations due to preliminary samples and tests. Geometric profile characteristics measured at the center (C) and edge (E) of the clear aperture are summarized in Table 1. Line depth around $b \approx 830$ nm associated with a short pitch $d \approx 260$ nm corresponds to an aspect ratio $b/d \approx 3.2$. This characterization confirms our capability to fabricate silica-based metamaterials with very large aspect ratios despite the small pitch required for operating in the UV spectral range.

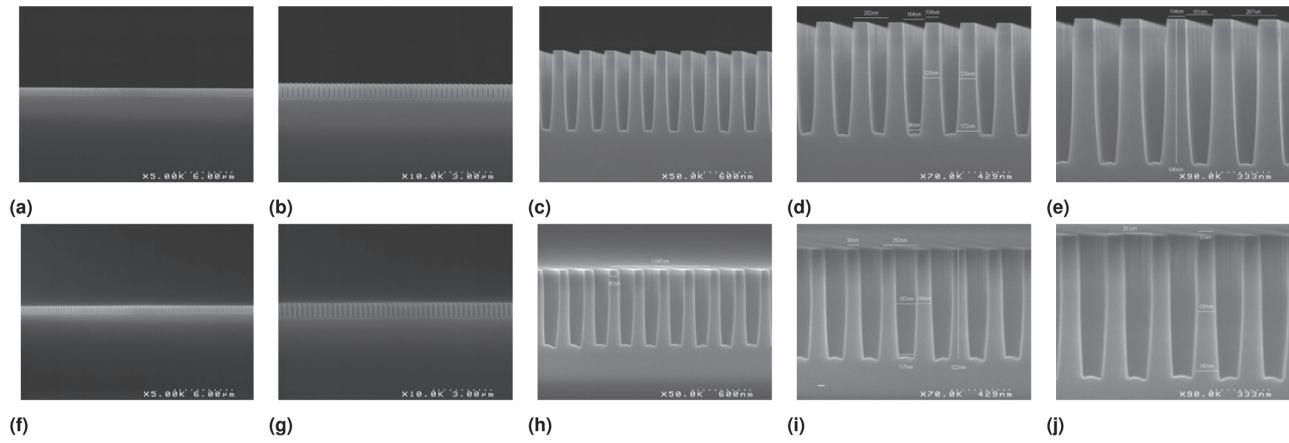


Fig. 4. SEM cross-section images at different magnifications on the center (top) and edge (bottom) of the clear aperture of the final metamaterial wave plate. The groove depths range between 820 nm and 840 nm, sidewall angle is about 87.5°, and line and space widths are detailed in Table 1.

Table 1. Metamaterial Wave Plate Profile Geometry from SEM Measurements Presented in Fig. 4^a

	Linewidth $d - c$ (nm)	Space Width c (nm)
Top	104 (C) - 93 (E)	164 (C) - 168 (E)
Bottom	172 (C) - 142 (E)	96 (C) - 117 (E)

^aValues are expressed in nanometers in the center (C) and on the edge (E) of the clear aperture for the top and bottom of the grating profile and compared to the prescription established in Section 2.

The period is estimated to $d \approx 268$ nm at the center (C) and $d \approx 260$ nm at the edge (E). The ratio DC between the linewidth c and the period d , $DC = 1 - c/d$, is estimated to $DC = 0.5148$ at the center, which is significantly different from the value considered in the numerical design ($DC = 0.4$). We will study in the next section the impact of this discrepancy in the period d and DC on the phase retardance and transmittance values.

B. Linear Retardance

The previous characterizations evidenced the conformity of the nanostructures with our specifications in terms of pillar height and pitch, with an offset on the DC. We now aim at characterizing the optical properties of the metamaterial wave plate in terms of linear phase retardance, transmission efficiency, and LIDT.

The linear phase retardance induced by the silica-based metamaterial was measured using an Exicor 450XT from Hind Instruments, Inc. The sample is measured in an ambient air environment with a 355 nm wavelength laser scanned over the grating clear aperture with a sampling step of 0.5 mm. Let us note the slight difference between the wavelength used for the linear retardance measurements, $\lambda = 355$ nm, and the operating wavelength, $\lambda = 351$ nm. This technique allows us to monitor the linear retardance performance over the surface with a spatial resolution of 0.5×0.5 mm². The 16 elements of the 4×4 Mueller matrix are measured by the experimental setup. The linear retardance is contained in the Mueller matrix, and we report in Fig. 5(a) its values over the 5×5 cm² surface of the grating. We first observe the homogeneity of the phase retardance over the surface. The mean value is 70.12 nm \pm 0.85 nm. This excellent homogeneity was expected after the observation of the profile homogeneity over the surface in SEM images (Fig. 4). This mean value of linear retardance corresponds roughly to a $\lambda/5$ wave plate. We will analyze later this result and quantify the influence of the

DC discrepancy on the linear retardance. At this step, one can conclude that the measurement of linear retardance evidences the ability of silica-based nanostructures to yield a linear retardance of $\lambda/5$ with excellent uniformity over the 5×5 cm² surface.

C. Transmittance

The second key parameter to measure is the optical transmittance that must be maximum since we consider here a metamaterial wave plate operating in transmission. We must avoid reflectance, which would be associated with a loss of energy at the focal spot of the final laser beam as well as energy diffracted in the $\pm 1^{\text{st}}$ orders. We measured the T^0 transmittance of the metamaterial wave plate using a photometer developed to measure transmission and reflection of large meter scale laser optics [42]. During the measurements, the wave plate is placed at normal incidence with an angular tolerance of 0.1° . The incident polarization is controlled with a tolerance of less than 1° . The clear aperture of the optical element is scanned at the wavelength of 351 nm with a small beam of 8 mm in diameter at 98% encircled energy and a sampling step of 2 mm. The minimal total uncertainty is estimated at 0.0042 with a confidence of more than 95% [43].

The results of transmittance are reported in Fig. 5(b). A mean transmission of 0.9159 is measured over the clear aperture. The scale of the color bar has been centered on the mean value to better visualize the distribution of transmittance over the surface. The small scale reveals the good uniformity of the transmittance with a RMS of 0.0059 over the 5×5 cm² clear aperture. The transmittance is slightly larger on the edges. This transmission value includes the contribution of the losses by reflection on the uncoated back side of the substrate (0.0369 at the wavelength of 351 nm). The mean transmission of the nanostructured wave plate is therefore 0.9509. This large transmittance and its good uniformity confirm the adequacy of the SEM measurements of the metastructure profile displayed in Fig. 4 with the specifications, in particular, the excellent homogeneity of the profile over the surface. At this stage, we assessed experimentally our ability to fabricate a silica-based metamaterial wave plate with a very high aspect ratio that combines a linear retardance of $\approx \lambda/5$, and a transmittance around 0.95 in the T^0 order. This value will have to be further increased to comply with high-power laser facilities such as NIF or LMJ. The solution will be found by slightly decreasing the period

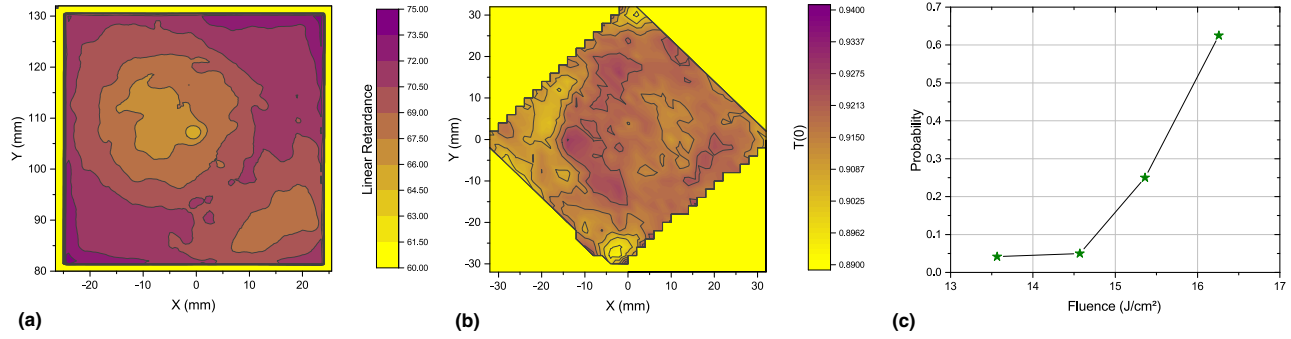


Fig. 5. Optical and laser damage characterization results. (a) Spatial distribution of the experimental retardance of the metamaterial wave plate. Measurement at normal incidence at the wavelength of 355 nm. A mean retardance of 70.2 nm is obtained with good uniformity. (b) Spatial distribution of the specular transmission T^0 at normal incidence at the wavelength of 351 nm. A mean diffraction efficiency of 0.9159 is obtained. (c) Laser induced damage probability measurement at the wavelength of 355 nm. Experiments are carried out in normal incidence with a pulse duration of 2.5 ns and a nanostructure placed on the front side with respect to the testing beam; a damage threshold of $13 \text{ J}/\text{cm}^2$ is measured.

down to 230 nm to avoid the propagation of non-specular ± 1 orders.

D. Laser Induced Damage Threshold

The third parameter to characterize is the resistance of the nanostructured glass to laser damages quantitatively characterized by LIDTs. Let us recall that the choice of silica was motivated by its high LIDT [44–46]. However, the large aspect ratios of nanostructures may decrease the resistance of glass nanostructures to laser damage. The metamaterial wave plate was tested with the nanostructured surface placed on the front side of the substrate with respect to the incoming testing beam. It was evidenced that the presence of grating lines favors damage growth after initiation [47], and this configuration was retained with success for the transmission grating of the final optic assembly of LMJ for similar reasons.

Damage resistance was measured using a setup dedicated to large scale optics operating at 351 nm. The frequency of a nano-second Nd:yag laser emitting at 1064 nm is first tripled to get a wavelength of 355 nm. The laser beam is then focused to irradiate the sample surface at the wavelength of 355 nm with a pulse duration of 2.5 ns and a beam diameter of $400 \mu\text{m}$ at $1/e$. Specific diagnostics are implemented on the setup to characterize the shot-to-shot beam spatial profile, the temporal profile of the laser irradiation, and the total energy deposited on the metamaterial wave plate. The presence of potential damage after each laser shot is monitored with a long working distance objective microscope with a resolution of $10 \mu\text{m}$. A full description of the setup is detailed in [48]. Damage probability is established by testing 30 damage sites with a single shot *per* site with fluences spanning the 13 to $17 \text{ J}/\text{cm}^2$ range. The measurements were performed on the polished substrate to qualify the damage resistance of the substrate prior to grating manufacturing.

Results established for the nanostructured glass are presented in Fig. 5(c). We can see that at 355 nm and for a 2.5 ns pulse duration, the wave plate exhibits a damage resistance of about $13 \text{ J}/\text{cm}^2$, while the polished substrates exhibit a damage resistance of $14 \text{ J}/\text{cm}^2$. This means that nanostructured glass, even with a high aspect ratio ($b/d \approx 3.2$), exhibits an LIDT only $1 \text{ J}/\text{cm}^2$ smaller than that exhibited by the polished glass substrate. This important result confirms the relevancy of glass to design metamaterial wave plates for high-power laser beams.

5. DISCUSSION AND CONCLUSION

The results displayed in Figs. 4 and 5 demonstrate the ability to etch $5 \times 5 \text{ cm}^2$ glass substrates with a short pitch around 268 nm and groove heights around 830 nm, estimated from SEM images, leading to aspect ratios larger than three. It turns out that this deeply nanostructured silica metamaterial yields a linear retardance of $\approx \lambda/5$. This value could be further improved to $\approx \lambda/4$ by decreasing the DC to 0.4 and by increasing the height of the silica pillars to 950 nm. However, the experimental value of the linear retardance of $70.12 \text{ nm} \pm 0.85 \text{ nm}$ will allow to manipulate light polarization and to create an elliptical polarization that will strongly decrease laser intensity heterogeneities. SEM measurements (see Section 3) evidenced that the DC is close to 0.5 instead of 0.4 (the DC value considered in the initial design) and that the period is close to 268 nm instead of 260 nm.

To estimate the impact of these deviations on linear retardance and transmission efficiency, we first plot in Fig. 6 the transmittance T^0 and phase retardance in air, $2\pi \Delta\phi/\lambda$, with respect to the DC. One can see that this deviation on the DC increases the transmission while shifting the linear retardance from 77 nm at DC = 0.4 to 65 nm at DC = 0.51.

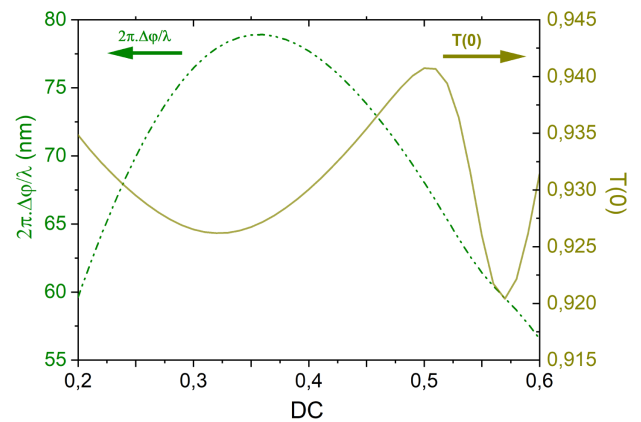


Fig. 6. Impact of the deviation in duty cycle on the optical performances of the metamaterial wave plate. Right ordinate axis: transmission efficiency T^0 in the zeroth order averaged over the fast and low axes and retardance in air between the components of the electric field parallel or perpendicular to the fast axis $2\pi \Delta\phi/\lambda$. Left ordinate axis: linear retardance in nm for a grating depth of $b = 830 \text{ nm}$ with respect to the duty cycle DC and period of 268 nm. Wavelength is $\lambda = 355 \text{ nm}$.

If the estimation of the DC is particularly challenging from SEM measurements, we can safely deduce from the comparison between experimental and numerical results that the discrepancy of the DC value and the high sensitivity of the linear retardance with respect to this parameter explains why the metamaterial acts like a $\lambda/5$ wave plate rather than the targeted $\lambda/4$ wave plate, which was the original objective. However, this value is large enough to significantly tailor the polarization properties of the laser beam. The conversion of linear to elliptical polarization will allow us to drastically reduce the heterogeneities of laser intensity over the target.

To conclude, this work reports the development of full-silica wave plates operating in the UV spectral range and exhibiting a high resistance to laser damage. We followed a CMOS compatible fabrication procedure to etch over the $5 \times 5 \text{ cm}^2$ surface high aspect ratio grooves, ~ 3 . The wave plate operates in the UV spectrum, which is privileged to bring light–matter interactions into high energy levels. The short wavelength imposes to associate the high aspect ratio with a short pitch, $\sim 260 \text{ nm}$. We report experimentally a phase retardance equivalent to a $\lambda/5$ wave plate. This value is associated with a high transmission efficiency, 95%, and importantly, a LIDT of 13 J/cm^2 , close to the value of 14 J/cm^2 , reported for the polished silica substrate. Such performances open the route towards the conversion of polarization of extremely intense UV lasers. This appealing application will require further developments, in particular (i) to fabricate full-sized optics compatible with large laser beams and (ii) to increase transmission efficiencies near 100%. (i) The process flow we used is currently scalable up to a clear aperture of 300 mm using standard CMOS equipment. However, fabrication of full-sized optics for high-power laser chains would rely on the processing of 450 mm wafers whose development is one of the most important challenges in micro-electronics [49]. The road map is well established, and this challenge attracts intense efforts in terms of funding and development. Alternatively, a process based on scanning beam lithography might also be developed since large-sized capabilities have already been demonstrated [50–53]. (ii) Transmission of the metamaterial phase plate will be increased by slightly reducing the pitch of the grating down to $d \sim 230 \text{ nm}$. This short period will prevent transmission in the ± 1 orders and promote further transmission in the zeroth order. Silica-based metamaterial wave plates will allow us to implement an original and reliable approach for smoothing the laser intensity over the focus area and for achieving unprecedented energy levels in light–matter interactions.

Funding. CEA - DAM Basic Science Research program.

Acknowledgment. The authors thank B. Hoffman and colleagues from the Laboratory for Laser Energetics, University of Rochester, USA, for Mueller matrix retardance measurements and T. Donval, C. Ameil, and L. Laignere from the Optical Metrology Laboratory, CEA Cesta, France, for laser damage testing and photometric measurements.

Disclosures. The authors declare no conflicts of interest.

Data Availability. Data underlying the results presented in this paper are not publicly available at this time but may be obtained from the authors upon reasonable request.

REFERENCES

- M. L. Spaeth, K. R. Manes, and D. H. Kalantar, *et al.*, "Description of the NIF laser," *Fusion Sci. Technol.* **69**, 25–145 (2016).
- J. Miquel, C. Lion, and P. Vivini, "The laser mega-joule: LMJ & PETAL status and program overview," *J. Phys. Conf. Ser.* **688**, 012067 (2016).
- T. Boehly, D. Brown, R. Craxton, R. Keck, J. Knauer, J. Kelly, T. Kessler, S. Kumpan, S. Loucks, and S. Letzring, "Initial performance results of the OMEGA laser system," *Opt. Commun.* **133**, 495–506 (1997).
- J. Kelly, L. Waxer, and V. Bagnoud, *et al.*, "OMEGA EP: high-energy petawatt capability for the OMEGA laser facility," *J. Phys. IV* **133**, 75–80 (2006).
- W. Zheng, X. Wei, and Q. Zhu, *et al.*, "Laser performance of the SG-III laser facility," *High Power Laser Sci. Eng.* **4**, e21 (2016).
- R. Lehmburg, A. Schmitt, and S. Bodner, "Theory of induced spatial incoherence," *J. Appl. Phys.* **62**, 2680–2701 (1987).
- S. Skupsky, R. Short, T. Kessler, R. Craxton, S. Letzring, and J. Soures, "Improved laser-beam uniformity using the angular dispersion of frequency-modulated light," *J. Appl. Phys.* **66**, 3456–3462 (1989).
- Y. Kato, K. Mima, N. Miyanaga, S. Arinaga, Y. Kitagawa, M. Nakatsuka, and C. Yamanaka, "Random phasing of high-power lasers for uniform target acceleration and plasma-instability suppression," *Phys. Rev. Lett.* **53**, 1057–1060 (1984).
- S. N. Dixit, I. M. Thomas, B. W. Woods, A. J. Morgan, M. A. Henesian, P. J. Wegner, and H. T. Powell, "Random phase plates for beam smoothing on the Nova laser," *Appl. Opt.* **32**, 2543–2554 (1993).
- J. Neauport, X. Ribeyre, J. Daurios, D. Valla, M. Lavergne, V. Beau, and L. Videau, "Design and optical characterization of a large continuous phase-plate for Laser Integration Line and Laser Megajoule facilities," *Appl. Opt.* **42**, 2377–2382 (2003).
- E. Lefebvre, R. Berger, A. Langdon, B. MacGowan, J. Rothenberg, and E. Williams, "Reduction of laser self-focusing in plasma by polarization smoothing," *Phys. Plasmas* **5**, 2701–2705 (1998).
- T. Boehly, V. Smalyuk, D. Meyerhofer, J. Knauer, D. Bradley, R. Craxton, M. Guardalben, S. Skupsky, and T. Kessler, "Reduction of laser imprinting using polarization smoothing on a solid-state fusion laser," *J. Appl. Phys.* **85**, 3444–3447 (1999).
- J. E. Rothenberg, "Polarization beam smoothing for inertial confinement fusion," *J. Appl. Phys.* **87**, 3654–3662 (2000).
- D. H. Edgell, P. B. Radha, J. Katz, A. Shvydky, D. Turnbull, and D. H. Froula, "Nonuniform absorption and scattered light in direct-drive implosions driven by polarization smoothing," *Phys. Rev. Lett.* **127**, 075001 (2021).
- J. Moody, B. MacGowan, J. Rothenberg, R. Berger, L. Divol, S. Glenzer, R. Kirkwood, E. Williams, and P. Young, "Backscatter reduction using combined spatial, temporal, and polarization beam smoothing in a long-scale-length laser plasma," *Phys. Rev. Lett.* **86**, 2810 (2001).
- S. Dixit, D. Munro, J. Murray, M. Nostrand, P. Wegner, D. Froula, C. Haynam, and B. MacGowan, "Polarization smoothing on the national ignition facility," *J. Phys. IV* **133**, 717–720 (2006).
- D. H. Munro, S. N. Dixit, A. B. Langdon, and J. R. Murray, "Polarization smoothing in a convergent beam," *Appl. Opt.* **43**, 6639–6647 (2004).
- X. Huang, H. Jia, W. Zhou, F. Zhang, H. Guo, and X. Deng, "Experimental demonstration of polarization smoothing in a convergent beam," *Appl. Opt.* **54**, 9786–9790 (2015).
- S. G. Demos, R. N. Raman, S. T. Yang, R. A. Negres, K. I. Schaffers, and M. A. Henesian, "Measurement of the Raman scattering cross section of the breathing mode in KDP and DKDP crystals," *Opt. Express* **19**, 21050–21059 (2011).
- K. Manes, M. Spaeth, and J. Adams, *et al.*, "Damage mechanisms avoided or managed for NIF large optics," *Fusion Sci. Technol.* **69**, 146–249 (2016).
- T. Kosc, H. Huang, T. Kessler, R. Negres, and S. Demos, "Determination of the Raman polarizability tensor in the optically anisotropic crystal potassium dihydrogen phosphate and its deuterated analog," *Sci. Rep.* **10**, 16435 (2020).
- T. Kosc, H. Huang, T. Kessler, A. Maltsev, and S. Demos, "Measurement of the angular dependence of the spontaneous Raman scattering in anisotropic crystalline materials using spherical samples: potassium dihydrogen phosphate as a case example," *Rev. Sci. Instrum.* **91**, 015101 (2020).
- T. Kosc, A. Kozlov, S. Papernov, K. Kafka, K. Marshall, and S. Demos, "Investigation of parameters governing damage resistance of nematic liquid crystals for high-power or peak-intensity laser applications," *Sci. Rep.* **9**, 16283 (2019).
- J. Oliver, C. Smith, and J. Spaulding, *et al.*, "Glancing-angle-deposited magnesium oxide films for high-fluence applications," *Opt. Mater. Express* **6**, 2291–2303 (2016).
- A. Drezet, C. Genet, and T. W. Ebbesen, "Miniature plasmonic wave plates," *Phys. Rev. Lett.* **101**, 043902 (2008).

26. Y. Zhao and A. Alù, "Manipulating light polarization with ultrathin plasmonic metasurfaces," *Phys. Rev. B* **84**, 205428 (2011).
27. A. Roberts and L. Lin, "Plasmonic quarter-wave plate," *Opt. Lett.* **37**, 1820–1822 (2012).
28. N. Yu, F. Aieta, P. Genevet, M. A. Kats, Z. Gaburro, and F. Capasso, "A broadband, background-free quarter-wave plate based on plasmonic metasurfaces," *Nano Lett.* **12**, 6328–6333 (2012).
29. A. Pors and S. I. Bozhevolnyi, "Efficient and broadband quarter-wave plates by gap-plasmon resonators," *Opt. Express* **21**, 2942–2952 (2013).
30. Y. Yang, W. Wang, P. Moitra, I. I. Kravchenko, D. P. Briggs, and J. Valentine, "Dielectric meta-reflectarray for broadband linear polarization conversion and optical vortex generation," *Nano Lett.* **14**, 1394–1399 (2014).
31. A. Arbabi, Y. Horie, M. Bagheri, and A. Faraon, "Dielectric metasurfaces for complete control of phase and polarization with subwavelength spatial resolution and high transmission," *Nat. Nanotechnol.* **10**, 937–943 (2015).
32. F. Ding, Z. Wang, S. He, V. M. Shalae, and A. V. Kildishev, "Broadband high-efficiency half-wave plate: a supercell-based plasmonic metasurface approach," *ACS Nano* **9**, 4111–4119 (2015).
33. S. M. Kamali, E. Arbabi, A. Arbabi, and A. Faraon, "A review of dielectric optical metasurfaces for wavefront control," *Nanophotonics* **7**, 1041–1068 (2018).
34. M. Nevière and E. Popov, *Light Propagation in Periodic Media: Differential Theory and Design* (CRC Press, 2002).
35. G. Bouchitte and R. Petit, "Homogenization techniques as applied in the electromagnetic theory of gratings," *Electromagnetics* **5**, 17–36 (1985).
36. E. Popov, S. Enoch, and N. Bonod, "Absorption of light by extremely shallow metallic gratings: metamaterial behavior," *Opt. Express* **17**, 6770–6781 (2009).
37. N. Bonod and J. Neauport, "Diffraction gratings: from principles to applications in high-intensity lasers," *Adv. Opt. Photon.* **8**, 156–199 (2016).
38. Y. Tang, C. Hooker, O. Chekhlov, S. Hawkes, J. Collier, and P. P. Rajeev, "Transmission grating stretcher for contrast enhancement of high power lasers," *Opt. Express* **22**, 29363–29374 (2014).
39. H. P. Howard, A. F. Aiello, J. G. Dressler, N. R. Edwards, T. J. Kessler, A. A. Kozlov, I. R. T. Manwaring, K. L. Marshall, J. B. Oliver, S. Papernov, A. L. Rigatti, A. N. Roux, A. W. Schmid, N. P. Slaney, C. C. Smith, B. N. Taylor, and S. D. Jacobs, "Improving the performance of high-laser-damage-threshold, multilayer dielectric pulse-compression gratings through low-temperature chemical cleaning," *Appl. Opt.* **52**, 1682–1692 (2013).
40. J. Neauport and P. Cormont, "Surface manufacturing and treatment," in *Laser-Induced Damage in Optical Materials* (CRC Press, 2014), pp. 332–357.
41. A. Kozlov, J. Lambropoulos, J. Oliver, B. Hoffman, and S. Demos, "Mechanisms of picosecond laser-induced damage in common multilayer dielectric coatings," *Sci. Rep.* **9**, 607 (2019).
42. S. Bouillet, C. Ameil, and V. Beau, *et al.*, "Large optics metrology for high-power lasers," *J. Opt. Soc. Am. A* **36**, C95–C103 (2019).
43. G. Gaborit, E. Lavastre, I. Lebeaux, and J.-C. Poncetta, "Specific photometer for large coated optics," *Proc. SPIE* **5878**, 58781A (2005).
44. M. Mero, A. J. Sabbah, J. Zeller, and W. Rudolph, "Femtosecond dynamics of dielectric films in the pre-ablation regime," *Appl. Phys. A* **81**, 317–324 (2005).
45. J. Neauport, E. Journot, G. Gaborit, and P. Bouchut, "Design, optical characterization, and operation of large transmission gratings for the Laser Integration Line and Laser Megajoule facilities," *Appl. Opt.* **44**, 3143–3152 (2005).
46. L. Gallais and M. Commandre, "Laser-induced damage thresholds of bulk and coating optical materials at 1030 nm, 500 fs," *Appl. Opt.* **53**, A186–A196 (2014).
47. M. Chambonneau and L. Lamaignère, "Multi-wavelength growth of nanosecond laser-induced surface damage on fused silica gratings," *Sci. Rep.* **8**, 891 (2018).
48. J. Neauport, L. Lamaignère, H. Bercegol, F. Pilon, and J.-C. Birolleau, "Polishing-induced contamination of fused silica optics and laser induced damage density at 351 nm," *Opt. Express* **13**, 10163–10171 (2005).
49. I. Kao and C. Chung, *Wafer Manufacturing: Shaping of Single Crystal Silicon Wafers* (Wiley, 2021).
50. T. Jitsuno, S. Motokoshi, and T. Okamoto, *et al.*, "Development of 91 cm size gratings and mirrors for LEFX laser system," *J. Phys. Conf. Ser.* **112**, 032002 (2008).
51. D. Ma, Y. Zhao, and L. Zeng, "Achieving unlimited recording length in interference lithography via broad-beam scanning exposure with self-referencing alignment," *Sci. Rep.* **7**, 926 (2017).
52. M. Li, X. Xiang, C. Zhou, and C. Wei, "Scan angle error measurement based on phase-stepping algorithms in scanning beam interference lithography," *Appl. Opt.* **58**, 2641–2649 (2019).
53. P. Müller, Y. Jourlin, C. Veillas, G. Bernaud, Y. Bourgin, S. H. Tonchev, and O. Dellea, "On-the-fly writing of a long grating phase mask," *Opt. Eng.* **50**, 038001 (2011).